



Bimodal grain sized barium titanate dielectrics enabled under the cold sintering process

Jake A. DeChiara ^{a b}, Sevag Momjian ^{a b}   , Ke Wang ^a, Clive A. Randall ^{a b}

Show more 

 Outline |  Share  Cite

<https://doi.org/10.1016/j.oceram.2024.100626> 

[Get rights and content](#) 

[Under a Creative Commons license](#) 

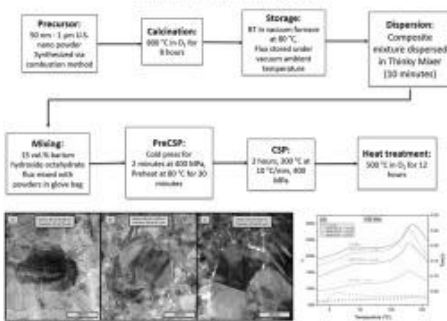
open access

Abstract

In barium titanate (BaTiO_3) the relative permittivity varies as a function of grain size due to the influence of various sizes and scaling effects. The cold sintering process (CSP) has been applied to sinter nanocrystalline BaTiO_3 ($<200\text{nm}$), however in conventionally sintered BaTiO_3 a maximum relative permittivity is achieved at average grain sizes around $0.8\mu\text{m}$. In this work the feasibility of cold sintering $1\mu\text{m}$ BaTiO_3 inclusions in ratios of fine-grained BaTiO_3 matrixes from 50 to 200 nm is investigated. Occurrences of both conformal sintering of inclusions into the matrix and constrained sintering with residual porosity are observed. Subsequently, electrical resistivities increased from $1 \times 10^8 \Omega\text{cm}$ to approximately $1 \times 10^{12} \Omega\text{cm}$ by a post CSP heat treatment of 500°C . Relative permittivity of annealed samples increases systematically following a logarithmic mixing law as a function of matrix grain size and increasing the ratio of inclusions to matrix.

Graphical abstract

Bimodal Grain Sized Composites of Barium Titanate Dielectrics Enabled Under the Cold Sintering Process



Download : [Download high-res image \(266KB\)](#)

Download : [Download full-size image](#)



Previous

Next



1. Introduction

Barium titanate (BaTiO₃) or BT, is a high permittivity ferroelectric perovskite ceramic with a wide range of technologically critical applications including Positive Temperature Coefficient Resistors (PTCR) and Multilayer Ceramic Capacitors (MLCCs) [[1], [2], [3]]. Control of the microstructure and of the final grain size distribution is a critical factor impacting the final electrical performance of barium titanate.

For capacitive applications, there is a balance that is required between the magnitude of the permittivity and the reliability. The reliability of the devices that are cofired into a multilayer ceramic capacitor (MLCC) is improved with the reduction of the grain size and increasing the number of grain boundary barriers to limit oxygen vacancy migration under an applied field [4]. However, below grain sizes of ~0.8 µm there are size effects from clamping of the domain walls which limit the dielectric response of a material [5]. Additionally, for grain sizes below 40 nm there are intrinsic size effects where the paraelectric-ferroelectric phase transition temperature renormalizes, and the depolarization fields suppress the onset of ferroelectricity [6].

A number of sintering methods have been applied to densify BT and other dielectric ceramics, such as flash sintering, spark plasma sintering, hot pressing, two-step sintering, rate-controlled sintering, atmosphere firing and liquid phase sintering [[7], [8], [9], [10], [11], [12], [13], [14]]. Despite advances in these sintering technologies, limitations imposed by the thermal processing parameters required to activate densification such as cost, sustainability, and microstructural control leave several outstanding challenges unaddressed [15]. With the additional needs for greater microstructural control and reducing processing temperatures, The Cold Sintering Process (CSP) becomes an attractive sintering technique for the fabrication of future electronic devices.

CSP is a relatively new sintering technique enabled by a non-equilibrium, pressure solution creep mechanism which permits the densification of ceramic materials at significantly reduced temperatures [16]. Densification by pressure solution creep is enabled when a powder compact is pressurized in the

presence of a transient fluid phase that the material is soluble in. This enhances the interfacial dissolution of matter at high pressure contacts between grains, and drives diffusion through chemical potential gradients, to lower pressure porous regions, resulting in precipitation of solute in the pores [17,18]. With densification of a diverse array of materials possible at temperatures below 300°C, the incorporation of organic polymers and non-noble metals into composite microstructures becomes feasible [19]. CSP can aid in enhancing the performance of dielectrics by adding low volume fractions of a high impedance polymer at the grain boundary which improves resistivity, nonlinear permittivity, reliability, and high field performance due to reduction of oxygen vacancy migration across the grain boundary [20].

Thus far, the CSP has been successfully employed to sinter fine grained barium titanate ranging in particle size from 50 to 200nm with finite but minimal grain growth [[21], [22], [23]]. In these size ranges, the relative permittivity of BT is decreased because of the size and scaling effects associated with the ferroelectric phenomena [24]. However, the microstructural control enabled by cold sintering enables the potential to incorporate a bimodal mixture of larger grain size inclusions to these smaller grain sized matrixes, to increase their dielectric performance while still preserving reliability. With traditional sintering the relative permittivity approaches a maximum at a particle size of ~800nm. The objective of this paper is to cold sinter barium titanate with a controlled bimodal mixture of fine grain barium titanate of 50, 100, and 200nm with 1µm inclusions, compare this to corresponding unimodal distributions, and investigate the consequences on the microstructure and electrical properties.

2. Experimental methodology

2.1. Precursor chemicals

BaTiO_3 powder (US Research Nanomaterials, Inc., 99.9% reported purity) synthesized by a combustion method with particle sizes ranging from 50nm to 1µm were sintered in this study.

Powders were calcined at 800°C under an oxygen atmosphere to remove organics and carbonates from the precursor powder surfaces. The precursor powder was mixed and ground in a mortar and pestle for 10min. Precursor powder and the final bulk samples were stored at 80°C under vacuum. $\text{BaOH}_2 \cdot 8\text{H}_2\text{O}$ (Alfa Aesar, 99.7% reported purity) was used as the transient chemical phase and stored under vacuum at room temperature to limit carbonate formation.

2.2. Particle preparation and mixing

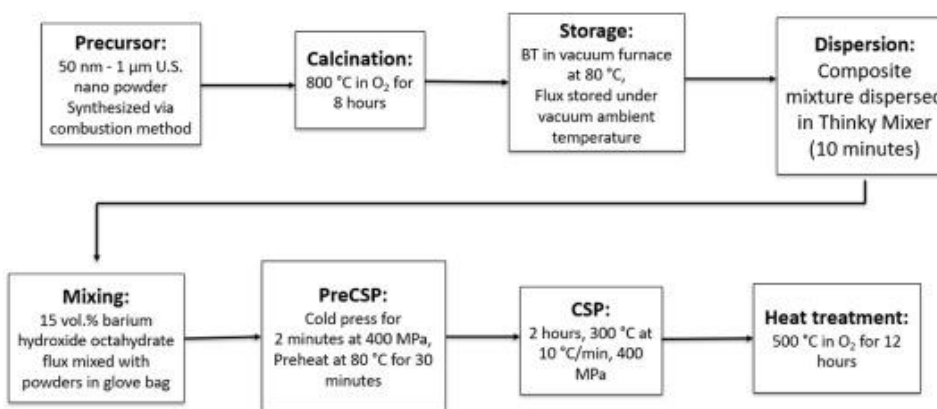
In this study, both monodispersed and bimodal mixtures were sintered. The monodispersed samples were barium titanate of 50, 100, and 200nm. The bimodal mixtures were, 80vol% of 50, 100, and 200nm barium titanate powders mixed with 20vol% of 1µm barium titanate. All samples had a total mass of 0.8g.

The bimodal mixtures were dispersed using a non-contact defoaming mixer (Thinky Corporation, model AR-250) for a total of 10min, with intermittent stops every minute to scrape powder adhering to the

container and to stir the powder. 15wt% of the $\text{BaOH}_2:8\text{H}_2\text{O}$ flux was then mixed with the precursor powder in a mortar and pestle for a total of 10min to disperse the flux.

2.3. Cold sintering procedure & post annealing

An Across International stainless-steel die with an inner diameter of 12.7mm was used to carry out the CSP. Inner spacers were machine polished to provide a flat surface for the application of pressure. Four inner spacers were used inside the die: two at the top and two at the bottom. Round nickel foil was punched and inserted onto the surface of the pucks to provide an inert surface during sintering. A heater jacket was wrapped around the die with a thermocouple inserted in between the jacket and die to detect sintering temperature. The powder and flux mixtures were initially pressed at 400MPa for 2min before CSP to form a green body. Pressure is released, and then transferred to a Carver press with heated plates. The green body is then pressed to 400MPa again. The heated plates, in tandem with the heater jacket (Tempco, band heater) are used to heat the system, with a thermal ramp rate of 10°C/min. The temperature is raised to 80°C (at which point the $\text{BaOH}_2:8\text{H}_2\text{O}$ melts) and held for 30min to allow for flux distribution, and then raised to 300°C and cold sintered for 2h. After cold sintering, the sample is brought down to room temperature and ejected. Fig. 1 shows a summary of the basic cold sintering process. The experimental procedures are all conducted in a temperature and relative humidity stable environment with the temperature being 20°C and a relative humidity of 70%. Following the cold sintering, the samples are then loaded into a furnace (Carbolite Gero, cube furnace), and heat treated at 500°C under oxygen atmosphere to increase resistivities.



Download : [Download high-res image \(225KB\)](#)

Download : [Download full-size image](#)

Fig. 1. Flow diagram of the cold sintering process adopted for this study.

2.4. Characterization

2.4.1. Density

Prior to annealing, the samples are sanded to a thickness of approximately 0.8mm, and geometric measurements are performed to calculate density. The ratio between the measured and theoretical

density of barium titanate ($\rho=6.02\text{ g/cm}^3$) is used to calculate the relative density of each sample.

2.4.2. Electrical measurements

Sputtering of 100nm platinum electrodes is performed in a rotary pumped coater (Quorum Technologies, model Q150R). Current-Voltage (I-V) measurements were carried out at voltages between 10 and 100V, and the slope of the curve, together with the geometry of the samples was used to calculate the resistivity of the dielectric. Impedance measurements were carried out after heating the samples at 150°C for 5min to limit the influence of adsorbed moisture on dielectric properties. Capacitance and dielectric loss were measured at frequencies of 10kHz and 100kHz in fixtures using an LCR meter (Keysight Precision LCR Meter, LXI) and temperatures between -20°C – 150°C using a delta oven. Samples were approximated as parallel plate capacitors, and electrode areas and sample thicknesses were used to determine relative permittivity. PE loops were measured at 10Hz and voltages between 10 and 60kV using a Sawyer-Tower circuit (Trek, model 609 A).

2.4.3. Microstructural characterization

Fractured surfaces were imaged via scanning electron microscopy (FESEM, Verios, Thermo Fisher Scientific) and energy dispersive spectroscopy (EDS). Thin cross-sectional transmission electron microscope (TEM) specimens were prepared by using focused ion beam (FIB, FEI Helios 660). The local microstructures of the cross-sectional samples were observed by FEI Titan3 G2 double aberration-corrected microscope at 300kV.

2.4.4. X-ray diffraction

X-ray diffraction was performed (XRD, Empyrean, PANalytical) with a scan step of 0.07°/s using Cu K α , scanning between 20°C and 80°C. XRD was carried out on cold sintered samples ground into powder along with a silicon internal standard. The precursor powder, and barium hydroxide octahydrate flux were also checked by XRD.

3. Results and discussion

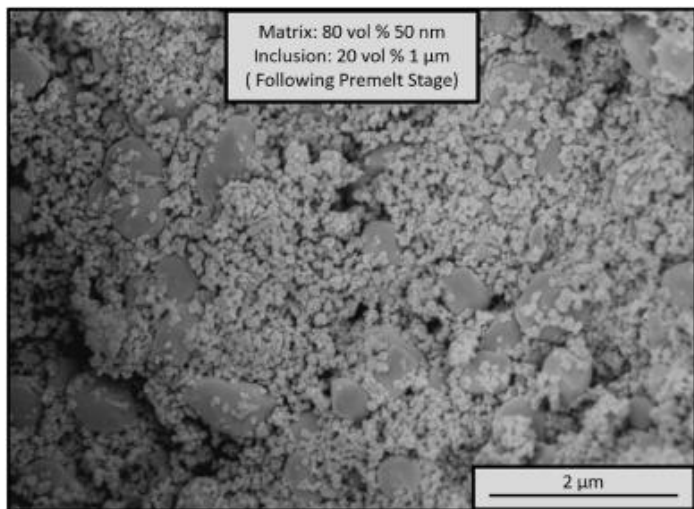
3.1. Powder processing to enable cold sintering of bimodal grain sized BaTiO₃

Earlier we described details of cold sintering of BT using both KOH–NaOH and BaOH₂·8H₂O transient phases [[20], [21], [22]]. Here we emphasize two additional aspects of importance, the surface chemistry with respect to BaCO₃, and maximizing the particle and transient chemistry prior to the cold sintering.

When sintering powders, it is important to understand surface chemistry, as this can be in the form of a BaCO₃ phase in the case of BT [25]. This is always important in high levels of industrial reproducibility of BT based capacitors. Surface chemistry is also critical in the cold sintering process, as it limits the kinetics of the low temperature diffusional processes that must be operational in the pressure solution mechanisms [26]. It is therefore important to ensure that there is no Barium Carbonate (BaCO₃) present

on the surface of the starting powder, as this can negatively impact the sintering and permittivity of BT. This is ensured by initially exposing the BT powders to an 800°C calcination.

Also crucial to densification, especially with a bimodal particle size mixture is the initial green body state of the sample. There is evidence suggesting that poor mixing of particles or inhomogeneous distribution of the flux can result in differential strains, causing macroscopic defects and poor densification [27]. The pre-pressing and pre-melting step aids in the formation of a more compact geometry and ensures further breaking of particle aggregates and improved densification [28]. In Fig. 2, a SEM images shows an example of uniform mixing of the BT powders after the mixing process, application of pressure, and pre-melting step at 80°C for an 80/20vol% mix of 50nm–1μm BT powder. Following the pre-melt step, there is also no surface impaction or faceting of the grains, indicating that no cold sintering, or diffusional pressure solution creep occurred at this stage [29].



[Download](#) : [Download high-res image \(451KB\)](#)

[Download](#) : [Download full-size image](#)

Fig. 2. Green body after the pre-melt stage. There is a rounded morphology in both 50nm and 1μm BT powder here in an 80/20 mix, indicative of just particle compaction without any sintering beyond the particle rearrangement densification.

After cold sintering at 300°C, the monodispersed 100nm and 200nm BT samples achieved densities of >93% which is consistent with final stage sintering behavior and comparable to densities achieved in previous CSP studies of BT powders in this size range [22]. However, the 50nm powder did not successfully densify because of mechanical failure during the sintering process which could be attributed to agglomeration during the particle mixing step resulting in inhomogeneous distribution of the flux. As a result, the relative densities in the 50nm case cannot be reported. A lower relative density of 80% was obtained in the pure 1 μm case, due to a lower driving force for sintering [30]. In all bimodal mixtures, relative densities of ~93% were obtained. These values are found in Table 2.

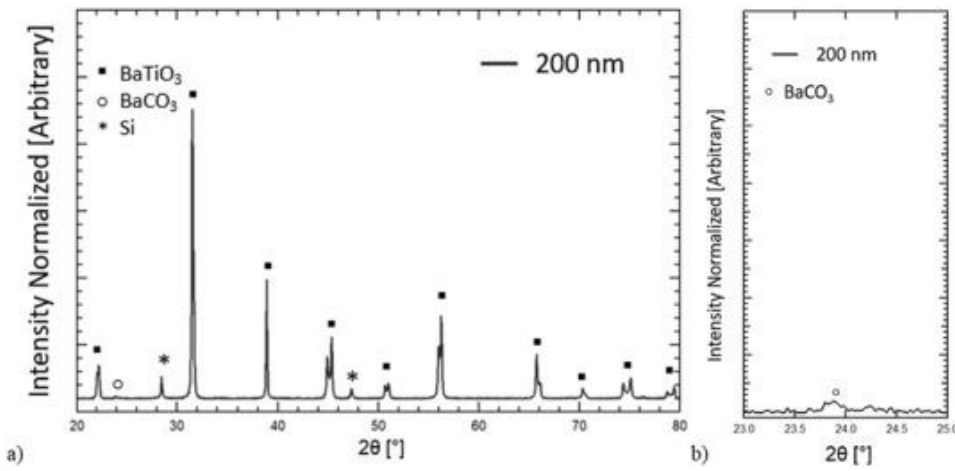
Table 1. Resistivity values for barium titanate processed with different temperatures.

Sample	Highest Processing Temperature, T (°C)	Resistivity, ρ(Ω*cm)	Reference
Cold Sintered BT-PTFE composite	225°C, BHO flux	1×10^{12}	[34]
Cold Sintered pure BT	225°C, BHO flux	1×10^8	[34]
Cold Sintered pure BT	500°C, oxygen atmosphere anneal	$2 \times 10^{12} - 9 \times 10^{12}$	This work
Conventionally sintered BT	1190–1320°C	$2 \times 10^{12} - 12 \times 10^{12}$	[35]

Table 2. Comparisons of the 500°C annealed cold sintered dielectrics of mono and bimodal BaTiO₃ ceramics.

Grain Size	$\epsilon_r(50^\circ\text{C}, 100\text{kHz})$ (Cold Sintered)	Tan(δ) 100kHz	T _c	γ	C (x 10 ⁵ K)	Relative density
1μm	2260	4.3%	134	1.75	39	80%
80/20 200nm – 1 μm	2125	3.1%	126	1.06	2.2	93.9%
80/20 100nm – 1 μm	1768	3.9%	128	1.15	0.45	93.8%
80/20 50nm – 1 μm	1237	2.9%	128	1.07	0.45	92.9%
200nm	800	2.8%	130	1.36	0.27	94.3%
100nm	900	3%	128	1.27	0.22	92.2%

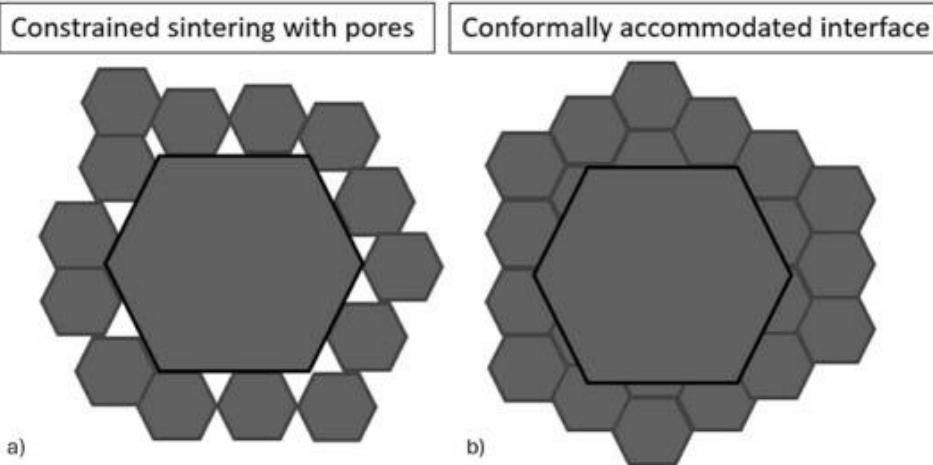
To assess the evolution of phases before and after cold sintering, X-ray diffraction was performed. Fig. 3 (a) presents a wide range 2θ XRD scan of a BT cold sintered sample of 200nm precursor powder. All BT peaks are present, but there is additionally a BaCO₃ peak around 2θ=23.8° as seen in Fig. 3 (b). The intensity of the peak increases with decreasing BT particle sizes, 200nm, 100nm and 50nm and increases with an increase in volume fraction of the nano particles relative to the 1.0μm BT (Fig. 3, Fig. 4, Fig. 5). It is inferred that there is a carbonate reaction between the water phase from the decomposition of the BaOH₂: 8H₂O and CO₂ from the air under the cold sintering process. The increase in surface area from increasing amounts of smaller particle sizes in the bimodal particle mixtures, increases the amount of the carbonate reaction. The BaCO₃ content being of lower permittivity in BaTiO₃ will lower the overall relative permittivity.



[Download](#) : [Download high-res image \(247KB\)](#)

[Download](#) : [Download full-size image](#)

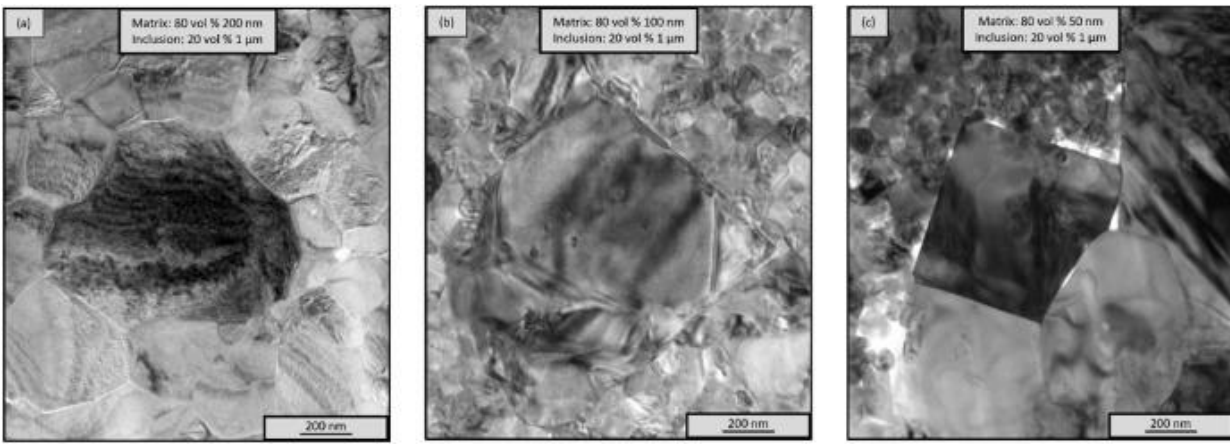
Fig. 3. (a) 2θ X-ray diffraction scan of a selected cold-sintered BaTiO_3 pellet (200nm precursor powder). BaTiO_3 peaks are marked with boxes, carbonate peaks are marked with open circles, Si peaks from a standard are marked with asterisks. (b) A close-up of the barium carbonate peak taken between $2\theta=23.0-25.0^\circ$.



[Download](#) : [Download high-res image \(290KB\)](#)

[Download](#) : [Download full-size image](#)

Fig. 4. A schematic illustrating sintering of large inclusions into a matrix phase. (a) Depiction of a large grain limiting shrinkage of the surrounding finer particles owing to constrained sintering at the interface and residual pores trapped at the interface. (b) Depiction of a case where creep diffusional processes dominate at the interface between the large and fine-grained particles resulting in a conformally accommodated interface between matrix and inclusion.



Download : [Download high-res image \(638KB\)](#)

Download : [Download full-size image](#)

Fig. 5. TEM bright field images of bimodal mixtures with varying matrix size. (a) 200 nm matrix with a conformally sintered interface with impaction onto an inclusion. (b) 100 nm matrix with conformally sintered interface without substantial impact on the inclusion. A morphological change of the inclusion into a cubic geometry is observed. (c) Constrained sintering with substantial porosity around an inclusion. A morphological change of the inclusion into a cubic geometry is observed. Other TEM micrographs are shown in Fig.S. (8) and (9).

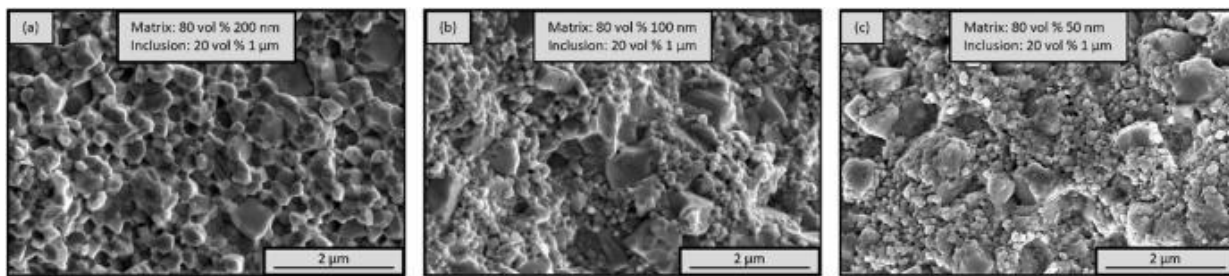
3.2. Characterization & microstructural analysis of cold sintered barium titanate bimodal ceramics

Before considering the reasons for microstructural development of the cold sintered bimodal mixtures, it is important to consider the risk of constrained sintering that could limit densification locally at the interfaces between the micron inclusions and nanoparticles within the matrix. Fig. 4 shows the basic concept of constrained sintering in bimodal particle size mixtures. Each of the larger particles potentially act as a constraining substrate to the surrounding small particles. Such constrained interfaces could limit the densification along these surfaces, as major densification must be normal to the interface. Earlier, a comprehensive review of constrained sintering was made by Green et al. [31]. From that review and subsequent studies [32], it is expected that samples sintered under constraints will display anisotropic macroscopic shrinkage and porosity evolution, thereby limiting the overall densification, and leaving residual porosity. However, with the pressure solution mechanism acting normal to the stressed constrained surfaces, densification along these surfaces is expected to be permitted. This provides microstructures with bimodal grains with limited porosity, high densities and is promising for the design of future cold sintered particle size mixtures and composites with constrained surfaces.

TEM imaging provides an excellent way to consider the interfaces between large and small grained BaTiO₃ particles undergoing cold sintering. With the 80 vol% of 100 nm and 200 nm-1 μ m BT particle mixtures, the interfaces are conformal because of the stress transfer around these interfaces via the pressure solution creep processes (Fig. 5. (a) and (b)). The interfaces are desirable as they remove a

major porosity source. The 80vol% 50nm - 1 μm interfaces however have a greater number of regions with porosity at their interfaces (Fig. 5 (c)). This is most likely because of poor distribution of the flux in the 50nm BT particles due to agglomeration.

The BT grain structures of the bimodal mixtures from SEM images are also presented. Fig. 6 compares the fracture surface of the 80vol % of 200, 100, and 50nm-1 μm BT particle size mixtures. The highest density structure is observed in the case of the 200nm-1 μm mixture case. These interfaces are additionally very well faceted, and conformal with minimal pitting. However, as seen in the TEM images, as the matrix particle size is decreased the surfaces become less conformal, and in the case of the 50nm-1 μm mixture, there is an increase in porosity because of the poorer distribution of the flux. With decreasing matrix particle size, there is also an increase in pitting within the 1 μm inclusions. Which is believed to be a result of stress amplifications against those regions (Fig.S14(c)), which accelerates dissolution in the direction normal to the stress (as noted in the conformally sintered interfaces). These features are additionally consistent with geologically observed pressure solution creep, in the pitting of pebbles within natural systems [17].

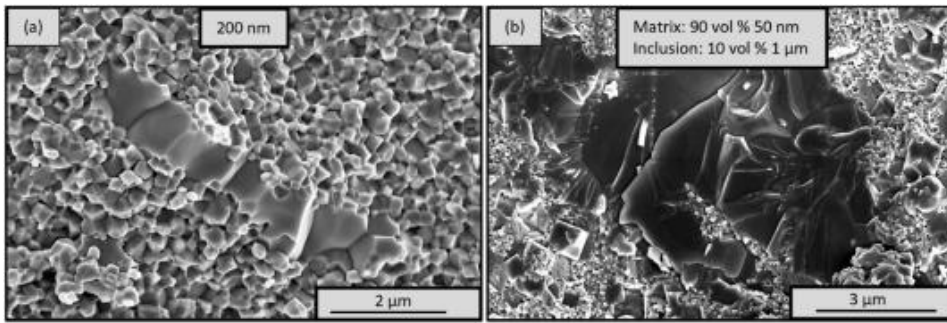


Download : [Download high-res image \(537KB\)](#)

Download : [Download full-size image](#)

Fig. 6. SEM images of 200nm 100nm, and 50nm matrix BT bimodal mixtures with volume fractions of 1 μm inclusions (80/20). There is good mixing of the grain sizes, the grain morphologies are faceted, and in the 1 μm grains there are indentations (surface holes) from the nanograin at the surfaces, a residual effect of pressure solution creep.

For completeness, we note that occasionally amongst several samples made, a highly unusual grain coarsening in isolated regions with elongated morphology was observed and is shown in Fig. 7 (a) and (b), Fig. S16. At this time, the origin of growth is not known, but it is suspected that enriched and trapped molten fluxes could drive the local grain growth. Additionally, there is still abnormal grain growth in the mono-particle cases. The rare event aspect of these observations means that we will not consider these in the following electrical analysis. However, as this is a surprising observation, we report it here in the hope that future researchers may bring light to the fundamentals of this mechanism.



Download : [Download high-res image \(478KB\)](#)

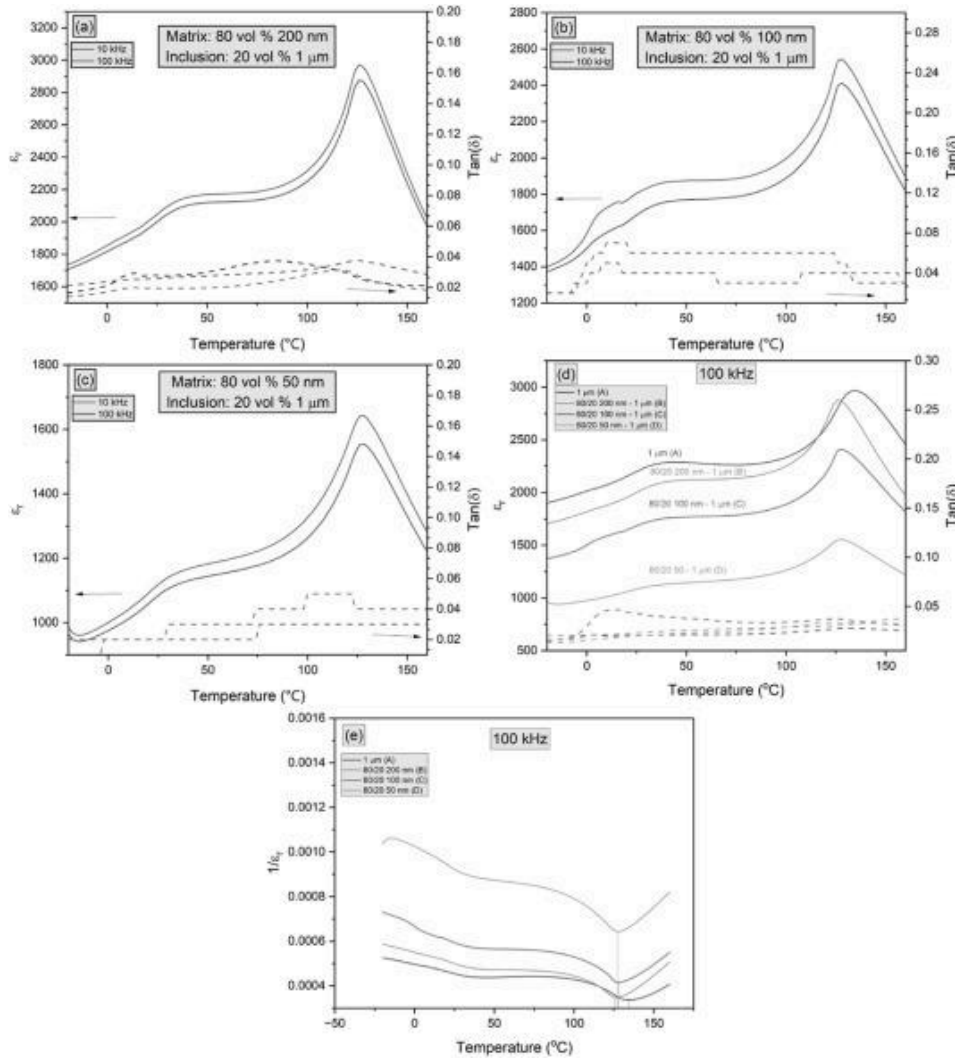
Download : [Download full-size image](#)

Fig. 7. SEM images demonstrating various examples of the unusual abnormal grain structure observed in cold sintered BaTiO₃ samples. (a) Elongated abnormal grain growth in a pure 200nm sample. (b) Coarsening is observed with growth encasing a portion of the 50nm matrix. Multiple growth processes are operating in this abnormal grain growth region.

3.3. Electrical properties of bimodal mixtures and dielectric trends

In previous studies of cold sintered barium titanate, reported resistivities were orders of magnitude lower than conventionally sintered barium titanate, as reported in Table 1. By applying a 500°C anneal in oxygen atmosphere for 12h, the resistivities of the cold sintered BaTiO₃ were substantially raised to those similar in literature. This annealing temperature is below that of which carbonates would decompose, and so the significant increase in resistivity could be due to enrichment of the grain boundaries with oxygen [33].

Fig. 8, and Fig.S10 show capacitance-temperature measurements that were then performed to determine the relative permittivity, dielectric loss, and Curie-Weiss behavior at 10kHz and 100kHz, over a temperature range from -20°C to 160°C.



Download : [Download high-res image \(697KB\)](#)

Download : [Download full-size image](#)

Fig. 8. (a-c) Temperature and frequency dependence of relative permittivity and dielectric loss for various particle mixtures. (d) Changes in relative permittivity and dielectric loss as a function of matrix combinations. Highest permittivity of the cold sintered samples is 1 μm and is ~90% dense, then a systematic decrease with 80/20 bimodal mixtures 200nm, 100nm and 50nm that are ~93% dense. (e) Curie-Weiss plot for the data in (d).

Comparing the bimodal mixtures to the monodispersed powders, an increase in relative permittivity is observed due to the average grain size approaching 0.8 μm . In the case of the monodispersed powders, the 1 μm sample exhibited the highest permittivity out of all samples. However, this was still below values reported in literature due to the high volume of porosity. The 100nm and 200nm BT demonstrated permittivity values comparable to those reported in literature, with slightly depressed permittivity, likely due to carbonates, and intergranular voids (S. 8) [36,37].

As seen in Table 2 and Fig. 8e, curie constants were additionally calculated and compared to reported literature values using a modified Curie-Weiss law [38]:

$$\frac{1}{\epsilon_r} - \frac{1}{\epsilon_m} = \frac{(T-T_C)^\gamma}{C} \quad (\text{eq.1})$$

where ϵ_r is the relative permittivity, ϵ_m is the maximum relative permittivity at the Curie temperature, C is the Curie-Weiss constant, and γ is the diffuseness degree. When γ is 1, a normal ferroelectric behavior is observed, while as γ approaches 2, relaxor ferroelectric behavior is measured. The γ value was calculated by linearizing the modified Curie-Weiss law and calculating the slope as reported in other work [38]. In this work, values of γ for bimodal mixtures were lower than that reported in other cold sintering studies, which may be due to experimental differences between these works [39]. In the mono sized particles, a substantially elevated γ is found with a depressed ϵ_r relative to expected values. It is likely that these deviations represent the presence of point defects from sources such as barium carbonate or residual flux after cold sintering which were unresolved by the current heat treatment. The residual space charge, the finite frequency dependence of the permittivity in the paraelectric regime and the small grains perturbs the magnitude of the Curie constant that would ideally be $2.5 \times 10^5 C$ particularly in the case for the $1 \mu\text{m}$ BT particles.

Finally, to then test whether the electrical measurements followed the initial bimodal size mixtures, a logarithmic mixing law (eq. 2) is used to track the increase in average relative permittivity from the $1 \mu\text{m}$ inclusions [40].

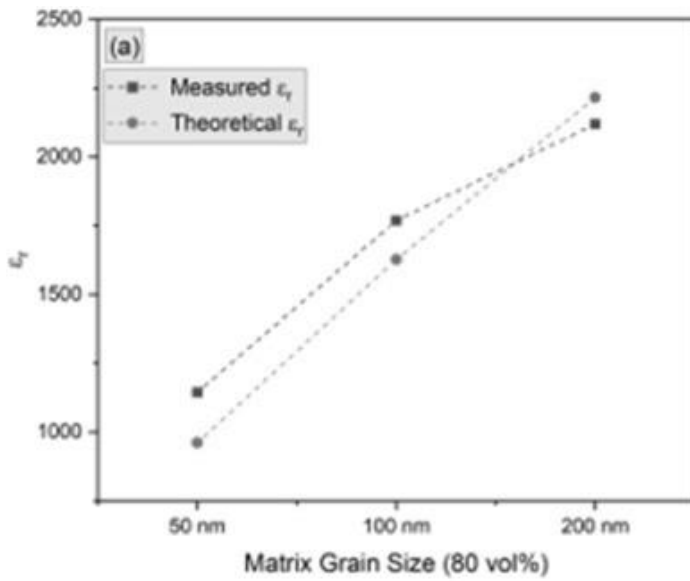
Here $\tilde{\epsilon}$, is based on the individual relative permittivity of each constituent phase, porosity and the volume fraction and permittivity of each of the i th phases given by f_i and $\epsilon_{r,i}$ respectively

$$\log \tilde{\epsilon} = \sum f_i \log \epsilon_{r,i} \quad (\text{eq.2})$$

The constituent phases of the bimodal mixtures will have a mixture of parallel and perpendicular connectivity between fine and large grain BaTiO_3 inclusions [41]. Additionally, there is assumed to be a random porosity associated with incomplete densification that also dilutes the permittivity and can be estimated from the relative density. As an approximation, the constituent phases are the large grained BaTiO_3 , finer grained BaTiO_3 , and the porosity with a relative permittivity of 1 (eq.3).

$$\log \tilde{\epsilon} = f_1 \log \epsilon_{r,1} + f_2 \log \epsilon_{r,2} + f_3 \log 1 \quad (\text{eq.3})$$

In our analysis, we take the relative permittivity of samples at 100kHz and 50°C . We assume the porosity volume fraction as 5 vol% to account for the variance in densities between the current work compared with those reported in the literature using various sintering techniques [24,36,37]. We take the trend of the average relative permittivity of the bimodal mixtures in 20/80 vol ratios with the matrix phase being the 80% phase for BaTiO_3 with 50, 100 and 200nm grain sizes, and the other 20% filler being the $1.0 \mu\text{m}$ particles, with 200nm and 100nm samples ~94% dense and 50nm samples ~93% dense. This gives a relative permittivity change of a factor of 2 between the extremes. The trend is consistent with eq.2, as shown in Fig. 9. The theoretical curve uses ϵ_r values of 1000 for 50nm, 2000 for 100nm, 3000 for 200nm, and 5000 for $1 \mu\text{m}$ [24].



Download : [Download high-res image \(184KB\)](#)

Download : [Download full-size image](#)

Fig. 9. Improvements in relative permittivity as a function of matrix size at constant inclusion volume. A theoretical model using the logarithmic mixing law accounting for 5 vol percent porosity is used to predict the expected permittivity of a bimodal mixtures using published values of conventionally sintered $1.0\mu\text{m}$ BT from literature [24].

The measured ϵ_r trends are generally in agreement with that predicted via the mixing law. In the theoretical analysis an expected increase in ϵ_r occurs as a function of matrix grain size due to the influence of the size and scaling effects. The measured ϵ_r shows slight deviations in shape from the mixing law, with the 200nm matrix mixtures showing a depressed ϵ_r which could be accounted for by intragranular voids (S.8) and localized barium carbonate at the grain boundaries. A slightly higher measured ϵ_r compared to prediction occurs in 50nm and 100nm matrix mixtures, indicating an overestimation of porosity or average grain size in our model. Despite slight deviations from the theoretical mixing law, this study demonstrates that controlled bimodal particle size mixtures of barium titanate can be successfully designed by the cold sintering process.

4. Conclusion and future work

In this study, the degree of control on morphological evolution by the cold sintering process was assessed with bimodal particle size mixtures. Through the pressure solution creep mechanism, densification of conformed surfaces was made possible, and the bimodal particle size distribution in dense bimodal mixtures was mostly preserved. It is important to note that rare events of abnormal grain growth were observed. Additionally, by pairing this with an annealing step, an increase in resistivity, and decrease in dielectric losses are achieved and compared to previous cold sintering studies. The dielectric properties in the $1\mu\text{m}$ monodispersed BT have high frequency dispersion with the cold sintering and this gives rise to an unrealistic Curie constant, C, due to the additional space charge contribution. With the bimodal BT mixtures this is suppressed and shows a Curie Constant that is more

intrinsic and with small grain sizes being impacted by the size and interfacial effects. Electrical performance of the relative permittivity was successfully enhanced by the incorporation of 1 μm grains, and followed trends proposed by a theoretical mixing law accounting for porosity.

Future work should explore alternative techniques for improving mixedness of the barium hydroxide octahydrate flux, as this made the sintering of finer grain BT more difficult. Additionally, while the abnormal grain growth could be partially explained by those areas being enriched by the barium hydroxide octahydrate, its presence in monodispersed cases questions this. While electrical properties demonstrated the preservation of a bimodal particle size distribution, values of relative permittivity were lower than literature due to carbonate formation and potential point defects. Alternative fluxes, sintering conditions including atmospheres, and post annealing strategies could be explored as potential solutions.

CRediT authorship contribution statement

Jake A. DeChiara: Writing – review & editing, Writing – original draft, Methodology, Investigation, Formal analysis, Data curation. **Sevag Momjian:** Writing – review & editing, Writing – original draft. **Ke Wang:** Investigation, Formal analysis. **Clive A. Randall:** Project administration, Methodology, Funding acquisition, Conceptualization.

Declaration of competing interest

The authors declare that they have no known competing financial interests or personal relationships that could have appeared to influence the work reported in this paper.

The author is an Editorial Board Member/Editor-in-Chief/Associate Editor/Guest Editor for [Journal name] and was not involved in the editorial review or the decision to publish this article.

The authors declare the following financial interests/personal relationships which may be considered as potential competing interests.

Acknowledgements

The authors would like to acknowledge Dean Anderson for his assistance in gathering the TGA/DSC data. We acknowledge and thank Dr. Zhongming Fan for performing preliminary TEM measurements in mixtures with 500nm inclusions which aided in establishing the feasibility of cold sintering bimodal barium titanate. J.D. is grateful to Dr. Tatiana Kuznetsova for feedback and recommendations regarding the graphical presentation of the XRD data used in this study. S.M. is grateful to Brittney Hawke for helpful grammatical edits. This work is based upon work supported by the National Science Foundation, as part of the Center for Dielectrics and Piezoelectrics under Grant Nos. IIP-1841466 and IIP-1841453, CR and SM are also partially supported by the National Science Foundation under the grant DMR-2202525.

References

[1] H. Kishi, Y. Mizuno, H. Chazono
Base-metal electrode-multilayer ceramic capacitors: past, present and future perspectives
Jpn. J. Appl. Phys., 42 (1R) (2003), p. 1
[View in Scopus](#) ↗ [Google Scholar](#) ↗

[2] O. Saburi
Properties of semiconductive barium titanates
J Physical Soc Japan, 14 (9) (1959), pp. 1159-1174
[View in Scopus](#) ↗ [Google Scholar](#) ↗

[3] W. Heywang
Resistivity anomaly in doped barium titanate
J. Am. Ceram. Soc., 47 (10) (1964), pp. 484-490
[CrossRef](#) ↗ [View in Scopus](#) ↗ [Google Scholar](#) ↗

[4] T. Baiatu, R. Waser, K. Härdtl
Dc electrical degradation of perovskite-type titanates: III, a model of the mechanism
J. Am. Ceram. Soc., 73 (6) (1990), pp. 1663-1673
[CrossRef](#) ↗ [View in Scopus](#) ↗ [Google Scholar](#) ↗

[5] M.H. Frey, Z. Xu, P. Han, D.A. Payne
The role of interfaces on an apparent grain size effect on the dielectric properties for ferroelectric barium titanate ceramics
Ferroelectrics, 206 (1) (1998), pp. 337-353
[CrossRef](#) ↗ [View in Scopus](#) ↗ [Google Scholar](#) ↗

[6] D. McCauley, R.E. Newnham, C.A. Randall
Intrinsic size effects in a barium titanate glass-ceramic
J. Am. Ceram. Soc., 81 (4) (1998), pp. 979-987
[CrossRef](#) ↗ [View in Scopus](#) ↗ [Google Scholar](#) ↗

[7] R. Shi, *et al.*
Flash sintering of barium titanate
Ceram. Int., 45 (6) (2019), pp. 7085-7089
 [View PDF](#) [View article](#) [View in Scopus](#) ↗ [Google Scholar](#) ↗

[8] D.F.K. Hennings, R. Janssen, P.J.L. Reynen
Control of liquid-phase-enhanced discontinuous grain growth in barium titanate
J. Am. Ceram. Soc., 70 (1) (1987), pp. 23-27
[CrossRef](#) ↗ [View in Scopus](#) ↗ [Google Scholar](#) ↗

[9] X. Deng, X. Wang, H. Wen, A. Kang, Z. Gui, L. Li
Phase transitions in nanocrystalline barium titanate ceramics prepared by spark plasma sintering
J. Am. Ceram. Soc., 89 (3) (2006), pp. 1059-1064
CrossRef ↗ View in Scopus ↗ Google Scholar ↗

[10] T. Karaki, K. Yan, M. Adachi
Barium titanate piezoelectric ceramics manufactured by two-step sintering
Jpn. J. Appl. Phys., 46 (10S) (2007), p. 7035
View in Scopus ↗ Google Scholar ↗

[11] L.A. Xue, Y. Chen, E. Gilbart, R.J. Brook
The kinetics of hot-pressing for undoped and donor-doped BaTiO₃ ceramics
J. Mater. Sci., 25 (1990), pp. 1423-1428
View in Scopus ↗ Google Scholar ↗

[12] A. V Ragulya
Rate-controlled synthesis and sintering of nanocrystalline barium titanate powder
Nanostruct. Mater., 10 (3) (1998), pp. 349-355
Google Scholar ↗

[13] N. Halder, D. Chattopadhyay, A. Das Sharma, D. Saha, A. Sen, H.S. Maiti
Effect of sintering atmosphere on the dielectric properties of barium titanate based capacitors
Mater. Res. Bull., 36 (5-6) (2001), pp. 905-913
 View PDF View article View in Scopus ↗ Google Scholar ↗

[14] M. Demartin, C. Hérard, C. Carry, J. Lemaître
Dedensification and anomalous grain growth during sintering of undoped barium titanate
J. Am. Ceram. Soc., 80 (5) (1997), pp. 1079-1084
CrossRef ↗ View in Scopus ↗ Google Scholar ↗

[15] T. Ibn-Mohammed, *et al.*
Decarbonising ceramic manufacturing: a techno-economic analysis of energy efficient sintering technologies in the functional materials sector
J. Eur. Ceram. Soc., 39 (16) (2019), pp. 5213-5235
 View PDF View article View in Scopus ↗ Google Scholar ↗

[16] A. Galotta, V.M. Sglavo
The cold sintering process: a review on processing features, densification mechanisms and perspectives

J. Eur. Ceram. Soc., 41 (16) (2021), pp. 1-17
View PDF View article View in Scopus ↗ Google Scholar ↗

[17] J.-P. Gratier, D.K. Dysthe, F. Renard
The role of pressure solution creep in the ductility of the Earth's upper crust
Adv. Geophys., 54 (2013), pp. 47-179
View PDF View article View in Scopus ↗ Google Scholar ↗

[18] X. Zhang, C.J. Spiers, C.J. Peach
Compaction creep of wet granular calcite by pressure solution at 28 C to 150 C
J. Geophys. Res. Solid Earth, 115 (B9) (2010)
Google Scholar ↗

[19] J. Guo, *et al.*
Recent progress in applications of the cold sintering process for ceramic–polymer composites
Adv. Funct. Mater., 28 (39) (2018), Article 1801724
View in Scopus ↗ Google Scholar ↗

[20] T. Sada, K. Tsuji, A. Ndayishimiye, Z. Fan, Y. Fujioka, C.A. Randall
Highly reliable BaTiO₃-Polyphenylene oxide nanocomposite dielectrics via cold sintering
Adv. Mater. Interfac., 8 (18) (2021), Article 2100963
View in Scopus ↗ Google Scholar ↗

[21] K. Tsuji, *et al.*
Single step densification of high permittivity BaTiO₃ ceramics at 300 °C
J. Eur. Ceram. Soc., 40 (4) (2020), pp. 1280-1284
View PDF View article View in Scopus ↗ Google Scholar ↗

[22] T. Sada, K. Tsuji, A. Ndayishimiye, Z. Fan, Y. Fujioka, C.A. Randall
High permittivity BaTiO₃ and BaTiO₃-polymer nanocomposites enabled by cold sintering with a new transient chemistry: Ba (OH) 2·8H₂O
J. Eur. Ceram. Soc., 41 (1) (2021), pp. 409-417
View PDF View article View in Scopus ↗ Google Scholar ↗

[23] N. Guo, H.-Z. Shen, P. Shen
One-step synthesis and densification of BaTiO₃ by reactive cold sintering
Scripta Mater., 213 (2022), Article 114628
View PDF View article View in Scopus ↗ Google Scholar ↗

[24] V. Buscaglia, C.A. Randall
Size and scaling effects in barium titanate. An overview

[25] MC Blanco-López, G. Fourlaris, B. Rand, F.L. Riley

Characterization of barium titanate powders: barium carbonate identification

J. Am. Ceram. Soc., 82 (7) (1999), pp. 1777-1786

[26] T. Sada, A. Ndayishimiye, Z. Fan, Y. Fujioka, C.A. Randall

Surface modification of BaTiO₃ with catechol surfactant and effects on cold sintering

J. Appl. Phys., 129 (18) (2021)

[27] A. Jabr, H.N. Jones, A.P. Argüelles, S. Trolier-McKinstry, C. Randall, R. Bermejo

Scaling up the cold sintering process of ceramics

J. Eur. Ceram. Soc., 43 (12) (2023), pp. 5319-5329, 10.1016/j.jeurceramsoc.2023.04.061 ↗

[28] M.J. Mayo

Processing of nanocrystalline ceramics from ultrafine particles

Int. Mater. Rev., 41 (3) (Jan. 1996), pp. 85-115, 10.1179/imr.1996.41.3.85 ↗

[29] A. Ndayishimiye, S.H. Bang, Christopher J. Spiers, C.A. Randall

Reassessing cold sintering in the framework of pressure solution theory

J. Eur. Ceram. Soc., 43 (1) (2023), pp. 1-13, 10.1016/j.jeurceramsoc.2022.09.053 ↗

[30] R.H.R. Castro, D. Gouvêa

Sintering and nanostability: the thermodynamic perspective

J. Am. Ceram. Soc., 99 (4) (Apr. 2016), pp. 1105-1121, 10.1111/jace.14176 ↗

[31] D.J. Green, O. Guillon, J. Rödel

Constrained sintering: a delicate balance of scales

J. Eur. Ceram. Soc., 28 (7) (2008), pp. 1451-1466

[32] E.A. Olevsky, B. Kushnarev, A. Maximenko, V. Tikare, M. Braginsky

Modelling of anisotropic sintering in crystalline ceramics

Phil. Mag., 85 (19) (2005), pp. 2123-2146

[33] G.Y. Yang, *et al.*

Oxygen nonstoichiometry and dielectric evolution of BaTiO₃. Part I—improvement of insulation resistance with reoxidation

J. Appl. Phys., 96 (12) (Dec. 2004), pp. 7492-7499, 10.1063/1.1809267 ↗

[View in Scopus ↗](#) [Google Scholar ↗](#)

[34] T. Sada, K. Tsuji, A. Ndayishimiye, Z. Fan, Y. Fujioka, C.A. Randall
Enhanced high permittivity BaTiO₃–polymer nanocomposites from the cold sintering process
J. Appl. Phys., 128 (8) (2020)
[Google Scholar ↗](#)

[35] H. Gong, X. Wang, S. Zhang, H. Wen, L. Li
Grain size effect on electrical and reliability characteristics of modified fine-grained BaTiO₃ ceramics for MLCCs
J. Eur. Ceram. Soc., 34 (7) (2014), pp. 1733-1739
 [View PDF](#) [View article](#) [View in Scopus ↗](#) [Google Scholar ↗](#)

[36] M.H. Frey, Z. Xu, P. Han, D.A. Payne
The role of interfaces on an apparent grain size effect on the dielectric properties for ferroelectric barium titanate ceramics
Ferroelectrics, 206 (1) (Feb. 1998), pp. 337-353, 10.1080/00150199808009168 ↗
[View in Scopus ↗](#) [Google Scholar ↗](#)

[37] G. Arlt, D. Hennings, G. de With
Dielectric properties of fine-grained barium titanate ceramics
J. Appl. Phys., 58 (4) (Aug. 1985), pp. 1619-1625, 10.1063/1.336051 ↗
[View in Scopus ↗](#) [Google Scholar ↗](#)

[38] K. Uchino, S. Nomura, L.E. Cross, S.J. Jang, R.E. Newnham
Electrostrictive effect in lead magnesium niobate single crystals
J. Appl. Phys., 51 (2) (Feb. 1980), pp. 1142-1145, 10.1063/1.327724 ↗
[View in Scopus ↗](#) [Google Scholar ↗](#)

[39] J.-P. Ma, X.-M. Chen, W.-Q. Ouyang, J. Wang, H. Li, J.-L. Fang
Microstructure, dielectric, and energy storage properties of BaTiO₃ ceramics prepared via cold sintering
Ceram. Int., 44 (4) (2018), pp. 4436-4441, 10.1016/j.ceramint.2017.12.044 ↗
 [View PDF](#) [View article](#) [View in Scopus ↗](#) [Google Scholar ↗](#)

[40] R.E. Newnham
Composite electroceramics
Ferroelectrics, 68 (1) (Jan. 1986), pp. 1-32, 10.1080/00150198608238734 ↗
[View in Scopus ↗](#) [Google Scholar ↗](#)

[41] A. V Polotai, A. V Ragulya, C.A. Randall

Preparation and size effect in pure nanocrystalline barium titanate ceramics

Ferroelectrics, 288 (1) (2003), pp. 93-102

Google Scholar ↗

Cited by (0)

© 2024 The Authors. Published by Elsevier Ltd on behalf of European Ceramic Society.



All content on this site: Copyright © 2024 Elsevier B.V., its licensors, and contributors. All rights are reserved, including those for text and data mining, AI training, and similar technologies. For all open access content, the Creative Commons licensing terms apply.

